Ras inhibitor CAPRI enables neutrophil-like cells to chemotax through a higher-concentration range of gradients

Xuehua Xu[a,1], Xi Wen[a], Amer Moosa[a], Smit Bhimani[a], and Tian Jin[a]

[a]Chemotaxis Signaling Section, Laboratory of Immunogenetics, National Institute of Allergy and Infectious Diseases, NIH, Rockville, MD 20852

Edited by Philipp Niethammer, Memorial Sloan-Kettering Cancer Center, New York, NY and accepted by Editorial Board Member Carl F. Nathan August 19, 2021 (received for review February 6, 2020)

Neutrophils sense and migrate through an enormous range of chemoattractant gradients through adaptation. Here, we reveal that in human neutrophils, calcium-promoted Ras inactivator (CAPRI) locally controls the GPCR-stimulated Ras adaptation. Human neutrophils lacking CAPRI (*capri*^{kd}) exhibit chemoattractant-induced, nonadaptive Ras activation; significantly increased phosphorylation of AKT, GSK-3α/3β, and cofilin; and excessive actin polymerization. *capri*^{kd} cells display defective chemotaxis in response to high-concentration gradients but exhibit improved chemotaxis in low- or subsensitive-concentration gradients of various chemoattractants, as a result of their enhanced sensitivity. Taken together, our data reveal that CAPRI controls GPCR activation-mediated Ras adaptation and lowers the sensitivity of human neutrophils so that they are able to chemotax through a higher-concentration range of chemoattractant gradients.

chemotaxis | adaptation | small GTPase Ras | GAP | CAPRI

Neutrophils provide first-line host defense and play pivotal roles in innate and adaptive immunity (1–3). The inappropriate recruitment and dysregulated activation of neutrophils contribute to tissue damage and cause autoimmune and inflammatory diseases (1, 4). Neutrophils sense chemoattractants and migrate to sites of inflammation using G protein–coupled receptors (GPCRs). To accurately navigate through an enormous concentration–range gradient of various chemoattractants (10^{-9} to $\sim10^{-5}$ M; *SI Appendix*, Fig. S1), neutrophils employ a mechanism called adaptation, in which they no longer respond to present stimuli but remain sensitive to stronger stimuli. Homogeneous, sustained chemoattractant stimuli trigger transient, adaptive responses in many steps of the GPCR-mediated signaling pathway downstream of heterotrimeric G proteins (5, 6). Adaptation provides a fundamental strategy for eukaryotic cell chemotaxis through large concentration–range gradients of chemoattractants. Abstract models and computational simulations have proposed mechanisms generating the temporal dynamics of adaptation: An increase in receptor occupancy activates two antagonistic signaling processes, namely, a rapid "excitation" that triggers cellular responses and a temporally delayed "inhibition" that terminates the responses and results in adaptation (5, 7–13). Many excitatory components have been identified during last two decades; however, the inhibitor(s) have just begun to be revealed (11, 14–17). It has been recently shown that an elevated Ras activity increases the sensitivity and changes migration behavior (18, 19). However, the molecular connection between the GPCR-mediated adaptation and the cell sensitivity remains missing.

The small GTPase Ras mediates multiple signaling pathways that control directional cell migration in both neutrophils and *Dictyostelium discoideum* (17, 20–24). In *D. discoideum*, Ras is the first signal event that displays GPCR-mediated adaptation (20). Ras signaling is mainly regulated through its activator, guanine nucleotide exchange factor (GEF), and its inactivator, GTPase-activating proteins (GAP) (16, 17, 25). In *D. discoideum*, the roles of DdNF1 and an F-actin–dependent, negative feedback mechanism have been previously reported (14, 17). We have previously demonstrated the involvement of locally recruited inhibitors that act on upstream of PI_3K in the sensing of chemoattractant gradients (11, 26). Recently, we identified a locally recruited RasGAP protein, C2GAP1, that is essential for F-actin–independent Ras adaptation and long-range chemotaxis in *Dictyostelium* (16). Active Ras proteins enrich at the leading edge in both *D. discoideum* cells and neutrophils (17, 27, 28). It has been reported that a RasGEF, RasGRP4, plays a critical role in Ras activation in murine neutrophil chemotaxis (21, 29). However, the components involved in the GPCR-mediated deactivation of Ras and their function in neutrophil chemotaxis are still not known.

In the present study, we show that a calcium-promoted Ras inactivator (CAPRI) locally controls the GPCR-mediated Ras adaptation in human neutrophils. In response to high-concentration stimuli, cells lacking CAPRI (*capri*^{kd}) exhibit nonadaptive Ras activation; significantly increased activation of AKT, GSK-3α/3β, and cofilin; excessive actin polymerization; and subsequent defective chemotaxis. Unexpectedly, *capri*^{kd} cells display enhanced sensitivity toward chemoattractants and an improved chemotaxis in low- or subsensitive-concentration gradients. Taken together, our findings show that CAPRI functions as an inhibitory component of Ras signaling, plays a critical role in controlling the

Significance

Neutrophils provide first-line host defense by migrating through chemoattractant gradients to the sites of inflammation. The inappropriate recruitment and misregulated activation of neutrophils contribute to tissue damage and cause autoimmune and inflammatory disease. One fascinating feature of chemotactic neutrophils is their ability to migrate through an enormous concentration range of chemoattractant gradients (10^{-9} to $\sim10^{-5}$ M) through "adaptation," in which cells no longer respond to the present stimuli but remain sensitive to stronger stimuli. The inhibitory mechanism largely remains elusive, although many molecules of the excitatory signaling pathway have been identified. Our study reveals that the inhibitory component, CAPRI, is essential for both the sensitivity and the GPCR-mediated adaptation of human neutrophils.

Author contributions: X.X. designed research; X.X. contributed new reagents/analytic tools; X.X., X.W., A.M., and S.B. performed research and analyzed data; and X.X. and T.J. wrote the paper.

The authors declare no competing interest.

This article is a PNAS Direct Submission. P.N. is a guest editor invited by the Editorial Board.

[1]To whom correspondence may be addressed. Email: xxu@niaid.nih.gov.

This article contains supporting information online at http://www.pnas.org/lookup/suppl/doi:10.1073/pnas.2002162118/-/DCSupplemental.

Published October 21, 2021.

concentration range of chemoattractant sensing, and is important for the proper adaptation during chemotaxis.

Results

CAPRI Regulates GPCR-Mediated Ras Adaptation in Human Neutrophils. Chemoattractants induce robust, transient Ras activation in mammalian neutrophils (21, 30). To identify which RasGAP proteins that deactivate Ras in neutrophils, we examined the expression of potential RasGAPs in mouse and human neutrophils (*SI Appendix*, Fig. S2*A*) (31, 32). We found that human and mouse neutrophils highly expressed CAPRI, also called RASA4, consistent with previous reports (33–35). The human neutrophil-like (HL60) cell line provides a useful model to study mammalian neutrophils (22, 36). The differentiated HL60 cell also highly expresses CAPRI (*SI Appendix*, Fig. S2*B*), consistent with a previous report (37), and provides a suitable cell system in which to study CAPRI's function in human neutrophils. We found that chemoattractant *N*-formyl-L-methionyl-L-leucyl-phenylalanine (fMLP) stimulation promoted the association between CAPRI and *N*-Ras/Rap1(Fig. 1*A*), suggesting a role of CAPRI in the regulation of chemoattractant-induced Ras and Rap1 signaling. To determine the function of CAPRI, we stably knocked down the expression of *capri* (*capri*^{kd}) in HL60 cells using *capri*-specific short hairpin RNA lentiviral particles (Fig. 1*B*). We first biochemically determined the dynamics of fMLP-induced Ras activation in both control (CTL) and *capri*^{kd} cells using a pull-down assay with a large population of cells (Fig. 1*C* and *SI Appendix*, Fig. S3). In resting *capri*^{kd} cells, there was a notably higher level of active Ras, indicating CAPRI's function in regulating basal Ras activity in the cells. In response to 10-μM fMLP stimulation, we detected a transient Ras activation followed by a secondary reactivation in CTL cells, as previously reported (14, 16, 30), but a significantly stronger, prolonged Ras activation in *capri*^{kd} cells (Fig. 1*D*). We further monitored fMLP-

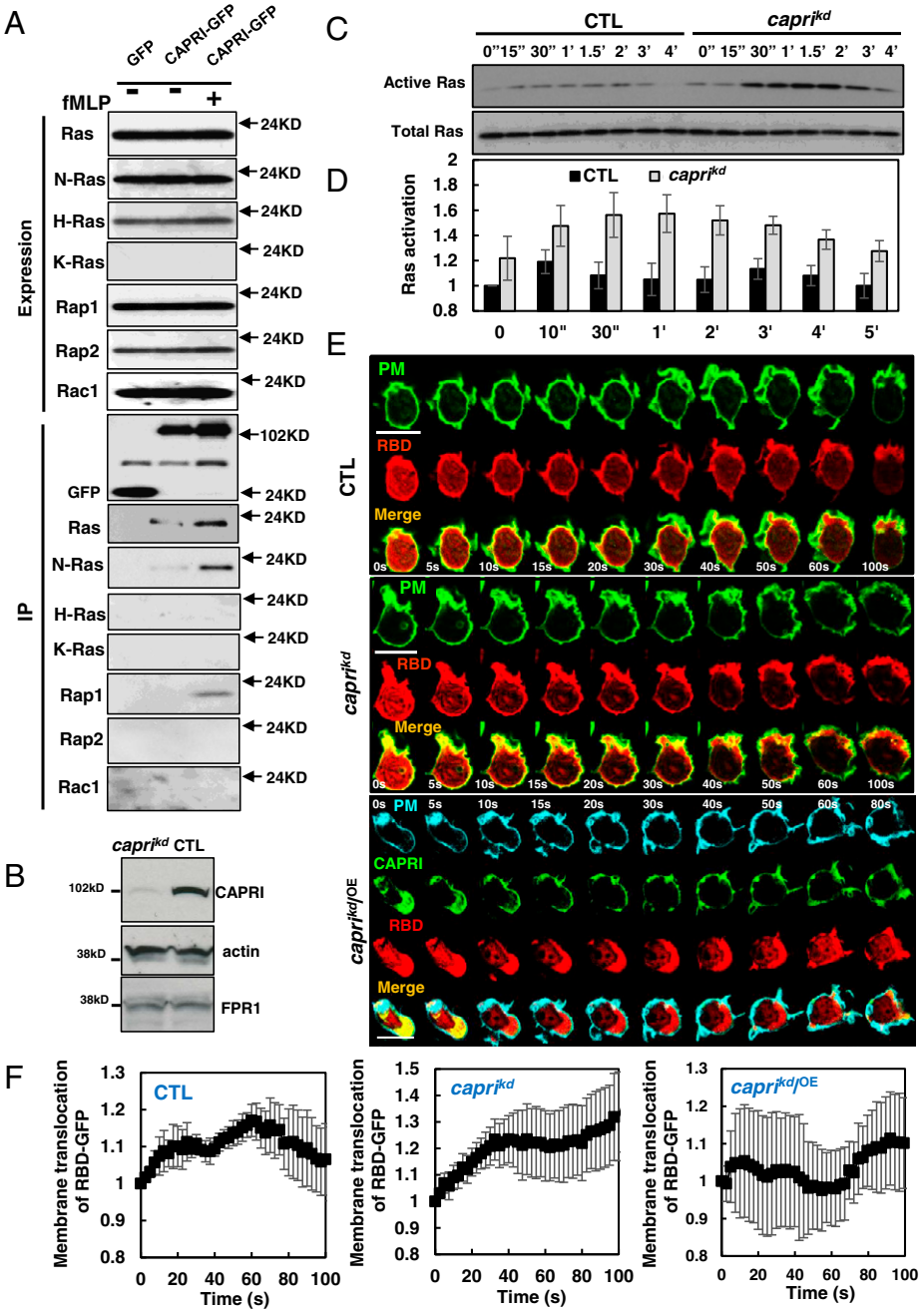

Fig. 1. CAPRI interacts with Ras and regulates chemoattractant GPCR-induced Ras adaptation. (*A*) fMLP-stimulated association between Ras/Rap1/Rac1 and CAPRI detected by coimmunoprecipitation assay. (*B*) Expression of *capri* in HL60 cells transfected with nonspecific (CTL) or *capri*-specific (*capri*^{kd}) short hairpin RNA virus particles. CAPRI was detected by antibodies against human CAPRI. Actin was detected as a loading control; fMLP receptor 1 FPR1 was also detected in both CTL and *capri*^{kd} cells. (*C*) fMLP-induced Ras activation in CTL and *capri*^{kd} cells determined by a pull-down assay. Upon stimulation with 10 μM fMLP at time 0", cells were collected, lysed at the indicated time points, and then centrifuged at 10,000 *g* for 10 min at 4 °C. Agarose beads preconjugated with RBD-GST (active RBD of Raf1 tagged with GST) were incubated with the supernatants of the lysates for 2 h at 4 °C then washed with lysis buffer. The protein bound to agarose beads was eluted with 2× SDS loading buffer (SLB). Aliquots of cells at the indicated time points were also mixed with the same volume of SLB for the detection of total Ras protein. The elutes of RBD-GST beads and the aliquots of the cells were analyzed by immunoblotting with anti-pan–Ras antibody to detect either active Ras or total Ras protein. (*D*) Normalized quantitative densitometry of the active Ras from three independent experiments, including the result presented in *C* and two independent measurements shown in *SI Appendix*, Fig. S3. The intensity ratio of active Ras and total Ras in WT at time 0 s was normalized to 1. Mean ± SD from the three independent experiments is shown. (*E*) Ras activation in CTL, *capri*^{kd}, and *capri*$^{kd/OE}$ cells monitored by the membrane translocation of the mRFP-tagged active RBD-RFP in response to 1-μM fMLP stimulation. CTL (*Top* and Movie S1, *Left*) and *capri*^{kd} (*Middle* and Movie S1, *Right*) cells expressed RBD-RFP (red) and a PM maker (green). The *capri*$^{kd/OE}$ cell (*Bottom* and Movie S2) is a *capri*^{kd} cell expressing a PM marker (cyan), CAPRI tagged with tGFP (CAPRI-tGFP, green), and RBD-RFP (red). fMLP was applied to the cells after 0 s. (Scale bar, 10 μm.) (*F*) The quantitative measurement of Ras activation as the membrane translocation of RBD-RFP in *E* is shown. Mean ± SD is shown; $n = 3$, 4, and 4 for CTL, *capri*^{kd}, and *capri*$^{kd/OE}$ cells, respectively.

induced Ras activation by visualizing the membrane translocation of a fluorescent, active Ras probe, the active Ras binding domain of human Raf1 tagged with RFP (RBD-RFP, red), in single live cells using fluorescence microscopy (Fig. 1*E*). In the present study, we used three plasma membrane (PM) markers, Mem-cerulean, C1AC1A-YFP, and CAAX-mCherry, to track the cell membrane in a live-cell experiment (*SI Appendix*, Fig. S4). We monitored Ras activation in CTL and *capri*^{kd} cells expressing both PM marker (green) and active Ras probe RBD-RFP (red) in response to uniformly applied 1-μM fMLP stimulation. We found that RBD-RFP translocated to and colocalized with PM marker (green) and then returned to the cytoplasm, followed by a second translocation to the protrusion sites of CTL cells (Fig. 1*E*, *Upper* and refer to Movie S1, *Left* for a complete, longer time period). In *capri*^{kd} cells, the same fMLP stimulation induced persistent membrane translocation and accumulation on the continuously expanding and broadened leading front of the cell (Fig. 1*E*, *Middle* and Movie S1, *Right*). To further examine CAPRI's function in Ras deactivation, we expressed CAPRI-tagged turboGFP (CAPRI-tGFP), RBD-RFP, and PM marker (Mem-cerulean) in *capri*^{kd} cells (*capri*$^{kd/OE}$) and monitored fMLP-induced Ras activation in these cells. The 1-μM fMLP stimulation triggered a clear membrane translocation of CAPRI-tGFP but much weaker or no membrane translocation of RBD-RFP in *capri*$^{kd/OE}$ cells (Fig. 1*E*, *Lower*, Movie S2, and *SI Appendix*, Fig. S5), suggesting that CAPRI translocates to the PM to inhibit Ras activation (33). Quantitative measurement of RBD-RFP membrane translocation confirmed that fMLP stimulation induced a biphasic Ras activation in CTL cells, as previously reported (30); a prolonged Ras activation in *capri*^{kd} cells; and a reduced Ras activation in *capri*$^{kd/OE}$ cells (Fig. 1*F*). Taken together, our results indicate that CAPRI is a RasGAP protein and is required for chemoattractant-mediated Ras adaptation in neutrophils.

Membrane Targeting of CAPRI in Response to Chemoattractant Stimulation. To reveal how CAPRI functions during neutrophil chemotaxis, we examined cellular localization of CAPRI-tGFP in HL60 cells. We found that CAPRI-tGFP colocalized with active Ras (RBD-RFP) and actin at the leading edge of chemotaxing HL60 cells in an fMLP gradient (Fig. 2*A*), consistent with previous reports (16, 22, 35). Chemoattractant fMLP and IL-8 induced the membrane translocation of CAPRI-tGFP (Fig. 1*E* and *SI Appendix*, Figs. S5 and S6). The G protein inhibitor pertussis toxin blocked the membrane translocation of CAPRI (*SI Appendix*, Fig. S7), indicating that chemoattractant GPCR/G protein–mediated signaling is required for CAPRI membrane targeting. To reveal the molecular mechanism of CAPRI membrane targeting, we investigated the domain requirement for its membrane translocation and interaction with Ras. We expressed tGFP-tagged wild type (WT) and mutants of ΔC2, ΔPH, and a GAP-inactive mutant R472A and determined their ability for Ras interaction (Fig. 2 *B* and *C* and *SI Appendix*, Fig. S8). We found that ΔC2 did not interact with Ras, and R472A showed a decreased interaction with Ras (Fig. 2*C*), consistent with previous reports (33, 38–41). We next monitored the membrane translocation ability of CAPRI WT and its mutant in response to fMLP stimulation (Fig. 2*D*). Upon fMLP stimulation, WT and R472A clearly translocated to and colocalized with PM marker (Fig. 2*D*, *Top* and Movie S3, *Top*), while ΔPH and ΔC2 showed significantly decreased or little membrane translocation (Fig. 2*D*, *Lower* and Movie S3, *Bottom*). Using total internal reflection fluorescent (TIRF) microscopy, we confirmed the membrane translocation behavior of CAPRI WT and its mutants (Fig. 2*E* and *SI Appendix*, Fig. S9) (42). Our results indicate that both the C2 and PH domains are crucial for chemoattractant-induced membrane targeting.

Chemoattractant Induces the Hyperactivation of Ras Effectors in *capri*^{kd} Cells. PI_3K-γ is a direct effector of Ras, which synthesizes lipid phosphatidylinositol (3–5)-trisphosphate [PtdIns(3–5)P_3, PIP_3] and activates the PIP_3-binding protein AKT in neutrophils (21, 29, 43). To examine the consequence of nonadaptive Ras activation, we monitored fMLP-induced PIP_3 production using a biosensor PH-GFP (PH domain of human AKT tagged with GFP, green) in both CTL and *capri*^{kd} cells (Fig. 3*A*) (44). We found that 1 μM fMLP trigged a robust translocation of PH-GFP to the entire PM, followed by a partial return to the cytosol and a gradual accumulation in the protrusion site of a CTL cell (Fig. 3*A*, *Upper* and Movie S4, *Left*). The same stimulation induced a stronger and persistent accumulation of PH-GFP all around the periphery of *capri*^{kd} cells (Fig. 3*A*, *Lower* and Movie S4, *Right*), indicating a hyperactivation of PI3K in cells lacking CAPRI. We further determined the activation profile of PI_3K-γ downstream effectors in CTL and *capri*^{kd} cells. AKT and GSK are well-known effectors of Ras/PI3K-γ signaling and are critical for the reorganization of actin cytoskeleton in neutrophil chemotaxis (22, 45). Therefore, we examined fMLP-induced PI3K-γ activation by measuring the phosphorylation of AKT on residues T308 and T473 in both CTL and *capri*^{kd} cells. We found that 1 μM fMLP triggered a transient phosphorylation on T308 and T473 of AKT in CTL cells, while it induced a persistent and significantly increased phosphorylation on both residues of AKT in *capri*^{kd} cells (Fig. 3 *B* and *C* and *SI Appendix*, Fig. S10), consistent with previous reports (46–48). Cofilin, an F-actin depolymerization factor, is essential for the depolymerization of F-actin in the dynamic reorganization of the actin cytoskeleton during cell migration (49). Its activity is regulated mainly through a phosphorylation event: phosphorylation on Ser-3 inhibits its actin binding, severing, and depolymerizing activities; and dephosphorylation on Ser-3 by slingshot proteins reactivates it. Slingshot 2 is a direct substrate of GSK3, and chemoattractants induce phosphorylation and the inhibition of GSK-3α/3β partially through PI3K-γ–AKT pathways in neutrophils (45). As previously reported (45), GSK-3α/3β is constitutively active and dephosphorylated in resting cells, and fMLP induced a transient phosphorylation and deactivation of GSK-3α/3β and led to a transient dephosphorylation of cofilin (Fig. 3 *D* and *E* and *SI Appendix*, Fig. S11). We found that 1-μM fMLP stimulation triggered a significantly stronger, prolonged phosphorylation of GSK-3α/3β and persistent dephosphorylation of cofilin in *capri*^{kd} cells. Taken together, these results indicate that CAPRI is essential for the proper activation/deactivation dynamics of the PI3K-γ/AKT/GSK3/cofilin signaling pathway in response to chemoattractant stimulations.

fMLP Stimulation Induces Increased Activation of Rap1 and Its Effector in *capri*^{kd} Cells. Rap1 is a close relative of Ras, initially described as a competitor of Ras by directly interacting with Ras effectors (50, 51). Later studies indicate that Rap1 also functions in independent signaling pathways to control diverse processes, such as cell adhesion, cell–cell junction formation, and cell polarity (52, 53). It has been shown that CAPRI also interacts with Rap1 in Chinese hamster ovary cells (54). We found that fMLP stimulation promoted the interaction between CAPRI and Rap1 in neutrophils (Fig. 1*A*) and that CAPRI was recruited to adhesion sites and colocalized with the PM marker during cell migration (*SI Appendix*, Fig. S12). We also noticed that chemoattractant stimulation induced the continuous expansion of *capri*^{kd} cells on the surface of the substratum, a typical feature of increased adhesion in the cells (Figs. 1*E* and 3*A*). To understand CAPRI's function in Rap1 activation, we determined fMLP-induced Rap1 activation in both CTL and *capri*^{kd} cells by a pull-down assay using the Rap-GTP binding domain of human RalGDS (RBD_{RalGDS}) (Fig. 4*A*). There was a higher level of active Rap1 in resting *capri*^{kd} cells. fMLP stimulation (1 μM) induced a transient Rap1 activation in CTL cells, while it triggered a significantly increased and prolonged Rap1 activation in *capri*^{kd} cells (Fig. 4*B*

CELL BIOLOGY

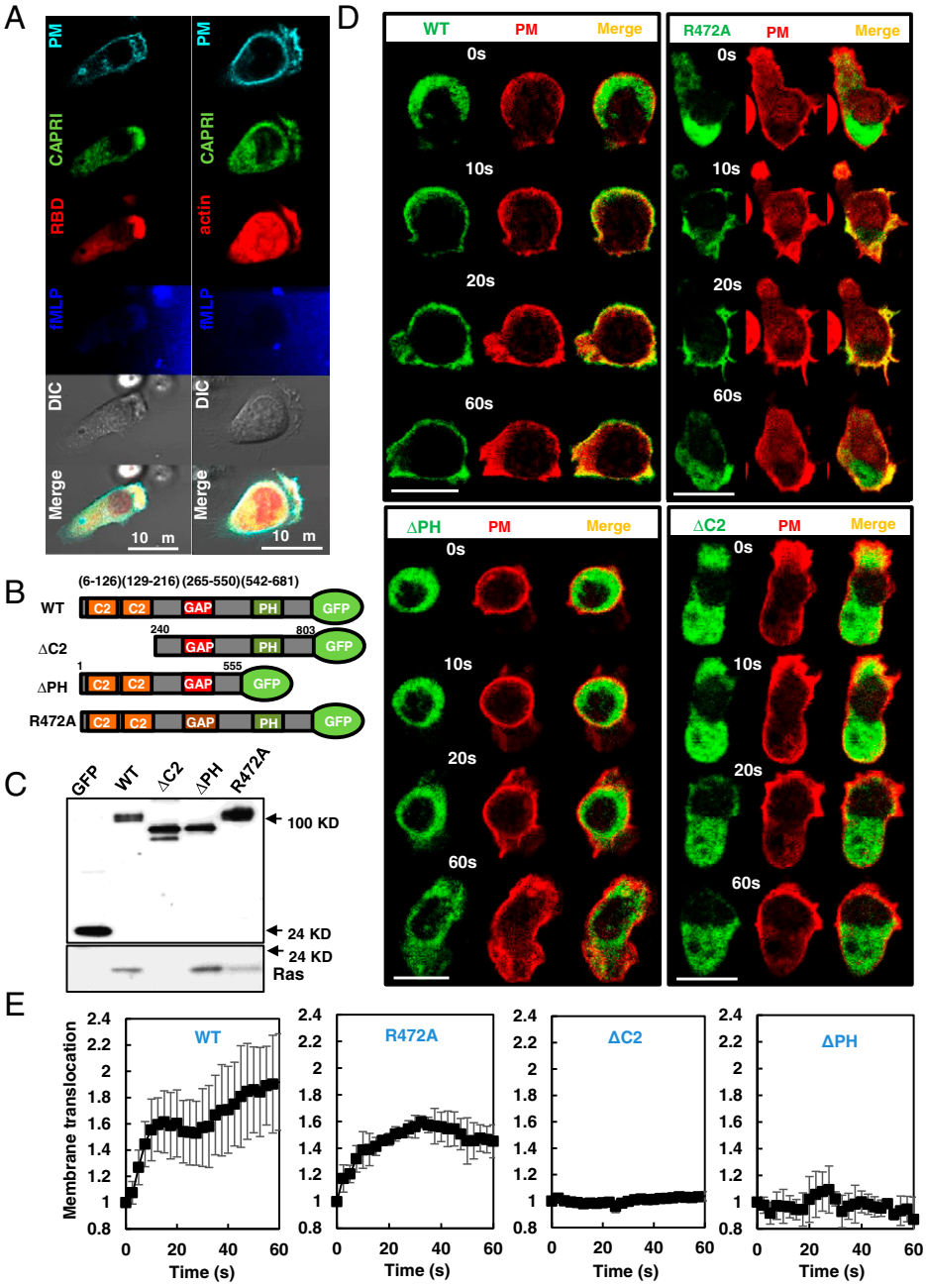

Fig. 2. Chemoattractant-induced membrane targeting of CAPRI. (*A*) Colocalization of active Ras and Rac1 with CAPRI in the leading edge of a chemotaxing cell. HL60 cells expressed a PM marker (cyan), both tGFP-tagged CAPRI (green), and RBD-RFP (red) or actin-mCherry (red) were exposed to a 100-nM fMLP gradient (dark blue) generated from a micropipette on the upper right side of the cells about 40 μm away. To visualize the fMLP gradient, 100 nM fMLP was mixed with Alexa 633 (dark blue). (Scale bar, 10 μm.) DIC (differential interference contrast) images are also shown. (*B*) The scheme shows the domain composition of tGFP-tagged WT or mutants of CAPRI. (*C*) Domain requirement for the interaction of CAPRI and Ras determined by coimmunoprecipitation. HL60 cells expressing either tGFP alone or tGFP-tagged WT or mutants of CAPRI were lysed with immunoprecipitation buffer with 1 mM GTP-γS and went through the coimmunoprecipitation process and Western blotting using anti-GFP or Ras antibodies. (*D*) Montage shows the membrane translocation of CAPRI and its mutants upon uniform application of 1 μM fMLP. Cells expressing tGFP-tagged WT or mutants of CAPRI (green) and PM marker (red) were imaged in time lapse, and 100 nM fMLP was homogeneously applied to the cells after 0 s. (Scale bar, 10 μm.) Movie S3 is CTL cells expressing PM marker (red) and tGFP-tagged WT (*Top Left*), R472A (*Top Right*), ΔPH (*Bottom Left*) or ΔC2 (*Bottom Right*) of CAPRI (green), respectively. (*E*) The quantitative measurement of the membrane translocation of CAPRI or its mutants is shown. Mean ± SD is shown, n = 5, 4, 4, and 4 for WT, ΔC2, ΔPH, or R472A of CAPRI, respectively. The quantitative measurement of intensity changes was described in *Materials and Methods*.

and *SI Appendix*, Fig. S13). We further monitored Rap1 activation using an active Rap1 probe, GFP-tagged RBD_{RalGDS} (RBD_{RalGDS}-GFP) (52), using live-cell fluorescence microscopy (Fig. 4*C*). We found that RBD_{RalGDS}-GFP colocalized with PM marker at the adhesion/protrusion sites of the resting cells (Fig. 4*C*), suggesting a potential function of Rap1 in the adhesion of neutrophils. Upon 1-μM fMLP stimulation, RBD_{RalGDS}-GFP (green) transiently translocated to and colocalized with PM marker (red), then returned to the cytoplasm, and then translocated to and colocalized with the PM marker again at the protruding sites of CTL cells (Fig. 4*C*, *Upper* and Movie S5, *Left*). In resting *capri*^{kd} cells, there were notably more membrane localizations of RBD_{RalGDS}-GFP, which is consistent with the notion that there is a higher, basal Rap1 activity in *capri*^{kd} cells (Fig. 4*C*, *Lower*). We further found that 1 μM fMLP triggered the prolonged translocation of RBD_{RalGDS}-GFP (green) to and colocalization with the PM marker (red) during a continuous expansion of *capri*^{kd} cells (Movie S5, *Right*), indicating a hyperactivation Rap1 and a consequently increased adhesion in the cells lacking CAPRI upon fMLP stimulation. To understand the effects of Rap1 hyperactivation, we examined Rap1 effector Erk42/44 phosphorylation (Fig. 4*D* and *SI Appendix*, Fig. S14). We detected higher, basal Erk42/44 phosphorylation in the nonstimulated *capri*^{kd} cells. In contrast to a rapid maximum phosphorylation of Erk 42/44 at 30 s in CTL cells, the same stimulation induced increasing dynamics of Erk42/44 phosphorylation in *capri*^{kd} cells (Fig. 4*E*), consistent with previous reports (33, 35, 54). Our results suggest that CAPRI deactivates Rap1 activation to facilitate an appropriate activation of Rap1 and its effector in adhesion and chemotaxis of neutrophils.

The Excessive Polymerization of Actin Impairs the Polarization and Migration of *capri*^{kd} Cells. The chemoattractant GPCR/G protein signaling regulates the spatiotemporal activities of Ras and Rap1 that mediate multiple signaling pathways to control the dynamics of actin cytoskeleton that drives cell migration. To evaluate the role of CAPRI in chemoattractant GPCR-mediated actin

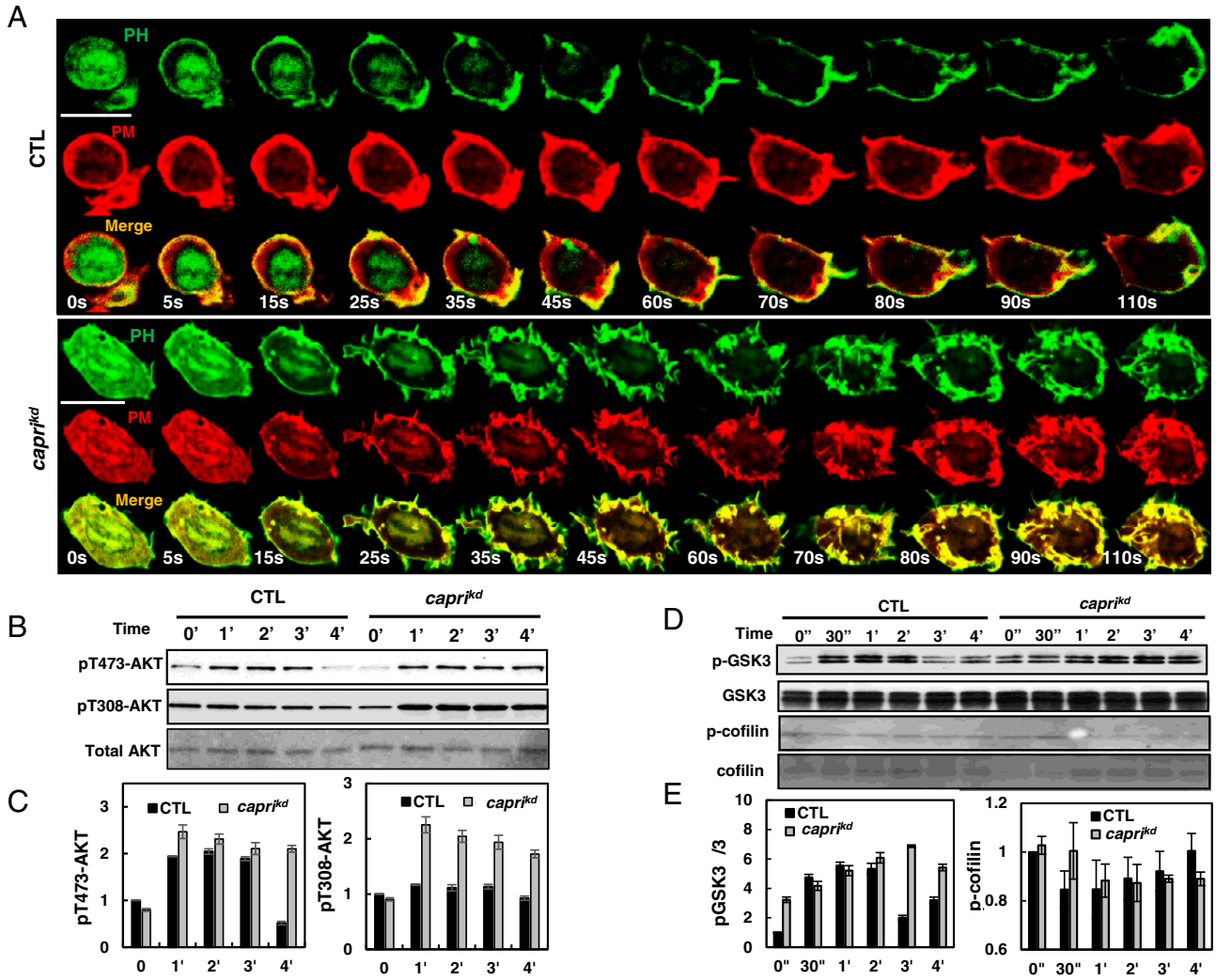

Fig. 3. Enhanced chemoattractant-induced activation of PI_3K signaling in *capri*^{kd} cells. (*A*) Montage shows the membrane translocation of PIP_3 biosensor PH-GFP in CTL and *capri*^{kd} cells in response to homogeneously applied 1-μM fMLP stimulation. Cells expressing PH-GFP (GFP-tagged PH domain of human AKT, green) and PM marker (red) were stimulated with 1 μM fMLP at time 0 s. (Scale bar, 10 μm.) Movie S4 is CTL (*Left*) and *capri*^{kd} (*Right*) cells, respectively. (*B*) fMLP-induced phosphorylation of AKT in CTL and *capri*^{kd} cells. A final concentration of 10-μM fMLP stimulation was added to the cells at time 0 s. Aliquots of cells were sampled at the indicated time points and subjected to the Western blot detection of the phosphorylated and total proteins of interest in *A* and *C*. (*C*) Normalized quantitative densitometry of phosphorylated AKT by total AKT protein in *B* and two independent measurements shown in *SI Appendix*, Fig. S10. Mean ± SD of the three independent experiments is shown. The intensity ratio of the phosphorylated versus total AKT in CTL cells at time 0 s is normalized to 1. (*D*) fMLP-induced phosphorylation of GSK-3α/3β and cofilin in CTL and *capri*^{kd} cells. (*E*) Normalized quantitative densitometry of the phosphorylated GSK-3α/3β and cofilin in *D* and two independent measurements shown in *SI Appendix*, Fig. S11. The intensity ratio of the phosphorylated versus total GSK-3α/3β and cofilin in CTL cells at time 0 s is normalized to 1. Mean ± SD of three independent experiments is shown.

assembly in neutrophils, we determined fMLP-mediated polymerization of actin in CTL and *capri*^{kd} cells using a centrifugation assay of actin filaments (F-actin) (Fig. 5*A*). In CTL cells, 10-μM fMLP stimulation induced a transient polymerization of actin. In *capri*^{kd} cells, the same stimulation also triggered the initial, transient actin polymerization followed by a much stronger and persistent actin polymerization (Fig. 5 *A* and *B*, and *SI Appendix*, Fig. S15). To understand the temporospatial dynamics of actin polymerization, we next monitored actin polymerization using the membrane translocation of an actin filament probe, F-tractin–GFP, in live cells by fluorescence microscopy (55). We found that, in response to uniformly applied 1 μM fMLP, F-tractin–GFP (green) translocated to and colocalized with the PM marker (red) along the entire periphery of CTL cells then withdrew and accumulated at the protruding sites of CTL cells (Fig. 5*C*, *Upper* and Movie S6, *Left*), indicating an initial, overall actin polymerization on the entire periphery, followed by a localized polymerization on the protrusion sites. In *capri*^{kd} cells, the same stimulation trigged a stronger and prolonged membrane translocation of F-tractin–GFP, followed by a slight withdrawal and then continuous accumulation on multiple expending/ruffling sites of cells (Fig. 5*C*, *Lower* and Movie S6, *Right*). To understand the effect of excessive actin polymerization on chemotaxis, we visualized the distribution of F-actin in cells migrating toward a 1-μM fMLP gradient using another F-actin probe (SiR-actin, a live-cell staining probe) (Fig. 5*D*). As expected, CTL cells displayed a clearly polarized actin polymerization: a protruding leading front (pseudopod) and a contracting trailing edge (uropod), and they chemotaxed through the gradient and accumulated at the source of the fMLP gradient (Fig. 5*D*, *Left* and Movie S7, *Left*). However, the *capri*^{kd} cells, especially those close to the source of the 1-μM fMLP gradient, displayed an overall excessive F-actin distribution, poor polarization, and significantly slow migration during chemotaxis (Fig. 5*D*, *Right* and Movie S7, *Right*). Notably, some

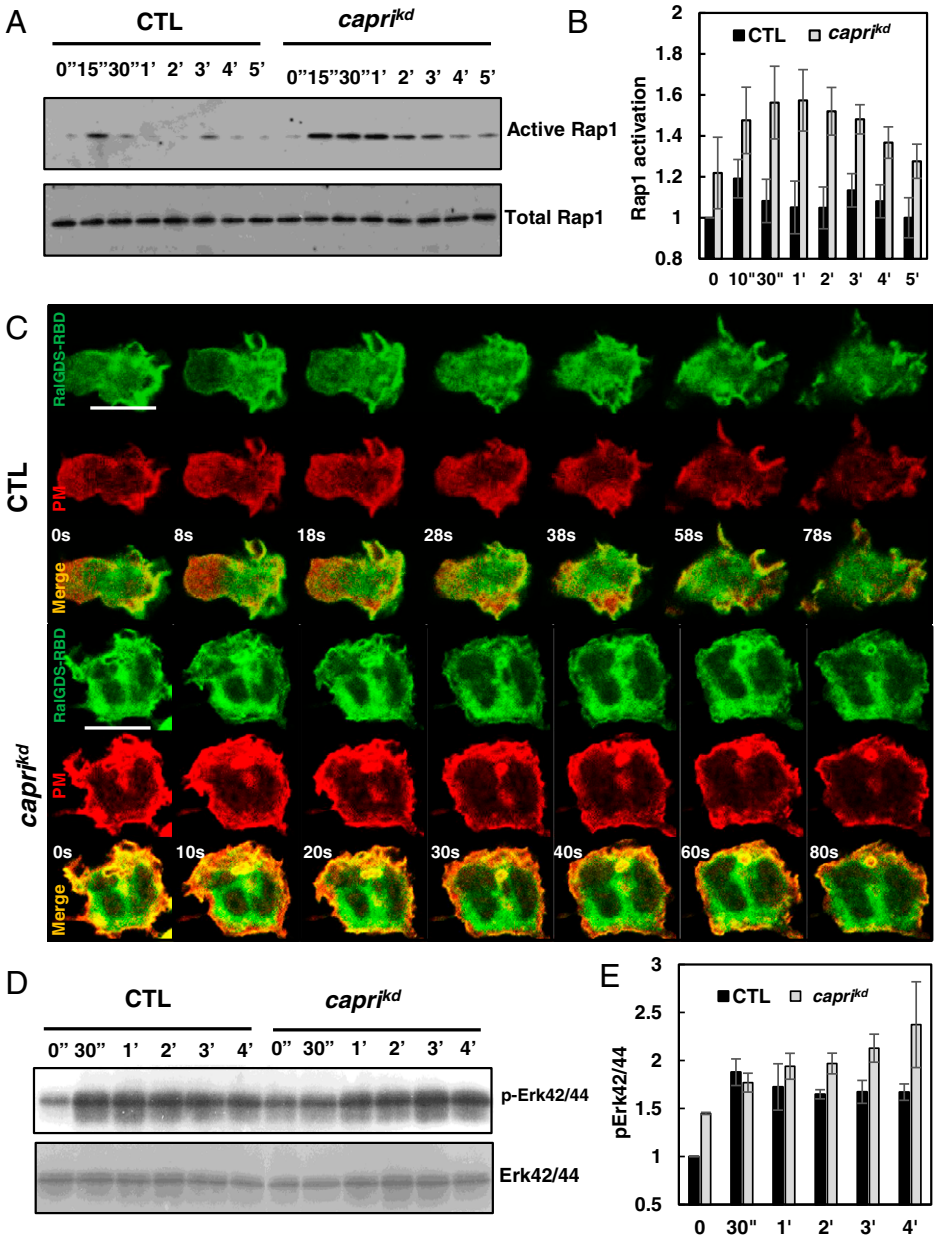

Fig. 4. Increased activation of Rap1 and its effector induced by fMLP stimulation in *capri*^{kd} cells. (*A*) fMLP-induced Rap1 activation in CTL and *capri*^{kd} cells determined by a pull-down assay using GST-RBD_{RalGDS} agarose beads. (*B*) Normalized quantitative densitometry of the active Rap1 in *A* and two independent measurements shown in *SI Appendix*, Fig. S13. The intensity ratio of active Rap1 and total Rap1 in WT at time 0 s was normalized to 1. Mean ± SD from the three independent experiments is shown. (*C*) fMLP-induced Rap1 activation monitored by the membrane translocation of the active Rap1 probe GFP-RBD_{RalGSD}. Cells expressing RBD_{RalGSD}-GFP (green) and PM marker (red) were stimulated with homogeneously applied 1 μM fMLP at 0 s. (Scale bar, 10 μm.) Movie S5 is a CTL (*Left*) and *capri*^{kd} (*Right*) cells, respectively. (*D*) fMLP-induced phosphorylation of Erk42/44 in CTL and *capri*^{kd} cells. (*E*) Normalized quantitative densitometry of the phosphorylated Erk42/44 in *E* and two independent measurements shown in *SI Appendix*, Fig. S14. The intensity ratio of the phosphorylated versus total Erk42/44 in CTL cells at time 0 s is normalized to 1. Mean ± SD of the three independent experiments is shown.

of the *capri*^{kd} cells located relatively far away from the source of fMLP showed polarized morphology and migrated effectively toward the fMLP source but gradually expended their leading front, eventually lost their polarity, and stopped moving when they were close to the source of the fMLP. The above results together indicate that chemoattractant stimuli at high concentrations induce excessive polymerization of actin and increased adhesion that impair the polarization and migration of *capri*^{kd} cells.

***capri*^{kd} Cells Display Improved Chemotaxis in Low- or Subsensitive-Concentration Gradients of Chemoattractants but Defective Chemotaxis in High-Concentration Gradients.** To further determine the function of CAPRI in the chemotaxis of neutrophils, we monitored the chemotaxis behavior of CTL and *capri*^{kd} cells in gradients of fMLP at different concentrations using an EZ-TAXIScan analysis (56). In a 1-μM fMLP gradient, *capri*^{kd} cells, in a clear contrast to CTL cells, displayed a significant decrease in migrating speed (CTL: 17.76 ± 3.37 μm/min; *caprikd*: 13.82 ± 2.90 μm/min), directionality (CTL: 0.88 ± 0.08; *caprikd*: 0.70 ± 0.11 μm/min), total path length (CTL: 164.64 ± 30.17 μm; *caprikd*: 90.70 ± 17.91 μm), and polarity, measured as roundness of a cell (percent) (CTL: 80.76 ± 8.12; *caprikd*: 87.14 ± 6.58) (Fig. 6 *A* and *B* and Movie S8). To understand chemotaxis behavior over a large concentration range, we further monitored the chemotaxis behavior of both CTL and *capri*^{kd} cells in the fMLP gradients at lower concentrations (Fig. 6*C*). We found that severe defects in chemotaxis in *capri*^{kd} cells were clearly observed when they experienced fMLP gradients at high concentration (>100 nM). When exposed to a gradient generated from a lower concentration (10 nM fMLP source), both CTL and *capri*^{kd} cells displayed similar directionality, although *capri*^{kd} cells still displayed decreased speed and total path length (Fig. 6*D* and Movie S9). In response to a gradient generated from a 1-nM fMLP source, *capri*^{kd} cells displayed significantly better directionality but similar migration speed, in comparison with CTL cells. In a 0.1-nM fMLP gradient, most CTL cells displayed random migration, while the majority of *capri*^{kd} cells displayed improved directionality and migration speed. Without a gradient, *capri*^{kd} cells displayed a bigger random walk compared to CTL cells. That is, *capri*^{kd} cells display defective chemotaxis in high-concentration gradients but improved chemotaxis in low- or subsensitive-concentration gradients of chemoattractants. We also observed this concentration-dependent change of chemotaxis capability of *capri*^{kd} cells in response to gradients of IL-8, another

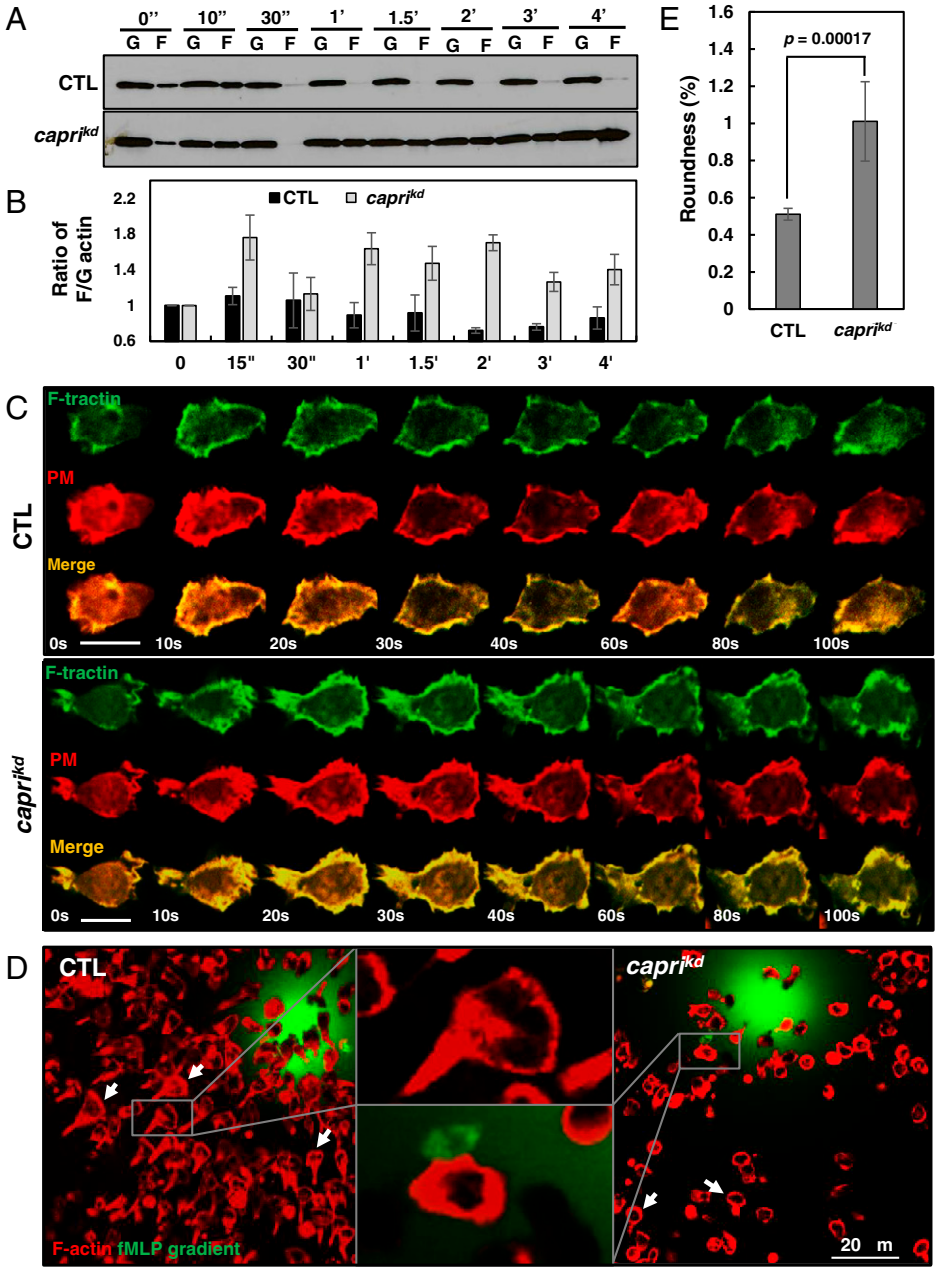

Fig. 5. Elevated polymerization of actin in response to a high concentration of fMLP stimulation impairs the polarity and migration of *capri*^{kd} cells. (*A*) The amount of globular (G) and filamentous (F) actin in CTL and *capri*^{kd} cells was determined by a centrifugation assay of F-actin. Cells were stimulated with 10 μM fMLP at time 0 s, and aliquots of cells at the indicated time points were analyzed. (*B*) Normalized quantitative densitometry of the F/G-actin ratio in the CTL and *capri*^{kd} cells in *A* and two sets of independent measurements shown in *SI Appendix*, Fig. S15. Mean ± SD from the three independent experiments is shown. The F/G ratio of CTL cells at 0 s was normalized to 1. (*C*) fMLP-induced actin polymerization by monitoring F-actin probe GFP–F-tractin using live-cell confocal microscopy in CTL and *capri*^{kd} cells. Cells expressing tractin-GFP (green) and PM marker (red) were stimulated with 1 μM fMLP at time 0 s. (Scale bar, 10 μm.) Movie S6 is a CTL (*Left*) and *capri*^{kd} (*Right*) cell, respectively. (*D*) F-actin distribution in chemotaxing CTL and *capri*^{kd} cells in a 1-μM fMLP gradient. The differentiated cells were stained with the actin filament probe, SiR-actin (red). Cells were exposed to a 1-μM fMLP gradient and allowed to chemotax for 5 min. Arrows point to the cells with a polarized, chemotaxing morphology. To visualize the gradient, 1 μM fMLP was mixed with fluorescent dye Alexa 488 (green, 1 μg/mL) and released from a micropipette at the center of the green fluorescent signal. (Scale bar, 20 μm.) Movie S7 is CTL (*Left*) and *capri*^{kd} (*Right*) cells, respectively. (*E*) The graph shows the roundness of CTL and *capri*^{kd} cells shown in *D*. The roundness was measured as the ratio of the width versus the length of the cell. That is, the roundness for a circle is 1 and for a line is 0. Student's *t* test was used to calculate the *P* value.

chemoattractant for neutrophils (*SI Appendix*, Fig. S16). The above result indicates that CTL cells chemotaxed efficiently through gradients of various chemoattractants ranging from 10^{-9} to 10^{-6} M, while *capri*^{kd} cells did so from 10^{-10} to 10^{-7} M.

An Increased Sensitivity of *capri*^{kd} Cells toward Chemoattractants. Using TIRF imaging, we noticed that CAPRI-tGFP localized on the membrane of resting cells, suggesting its potential role in inhibiting basal Ras activity (Fig. 7*A*). As expected, fMLP stimulation induced a strong, quick membrane translocation of CAPRI followed by a slow, gradual withdrawal with a notable fraction of CAPRI remaining on the PM for quite a long period of time. We also observed a higher, basal Ras activity in *capri*^{kd} cells (Fig. 1*C*), indicating a potential role of CAPRI in maintaining a low, basal Ras activity in the resting cells. The basal activity of Ras is part of a positive feedback mechanism that promotes actin dynamics and, more importantly, chemotaxis in a shallow chemoattractant gradient in *D. discoideum* (24). We speculated that the higher, basal Ras activity in *capri*^{kd} cells might contribute to their enhanced random walk without a gradient or to their improved chemotaxis in a low- or subsensitive-concentration gradient (Fig. 6). To determine whether *capri*^{kd} cells have become more sensitive to the stimulus, we determined Ras and Rap1 activation in response to fMLP stimulation at different concentrations using a pull-down assay (Fig. 7*B*). Comparing to the CTL cells, we detected a stronger Ras/Rap1 activation in *capri*^{kd} cells in response to all three different concentrations (Fig. 7*C* and *SI Appendix*, Fig. S17). In response to 0.1-nM fMLP stimulation, CTL cells did not show a clear Ras or Rap1 activation but displayed a weak oscillation, while *capri*^{kd} cells showed a clear, transient Ras activation. In response to 10-nM and 1-μM fMLP stimulation, *capri*^{kd} cells showed a stronger, longer activation of both Ras and Rap1 than CTL cells did.

We further determined the responsiveness of both CTL and *capri*^{kd} cells to either 0.1-nM or 10-nM fMLP stimulation by monitoring actin polymerization through the membrane translocation of F-tractin–GFP (Fig. 8). In response to 0.1-nM fMLP stimulation, most CTL cells (~90%) did not show the clear membrane translocation of F-tractin–GFP to the PM, while they showed a

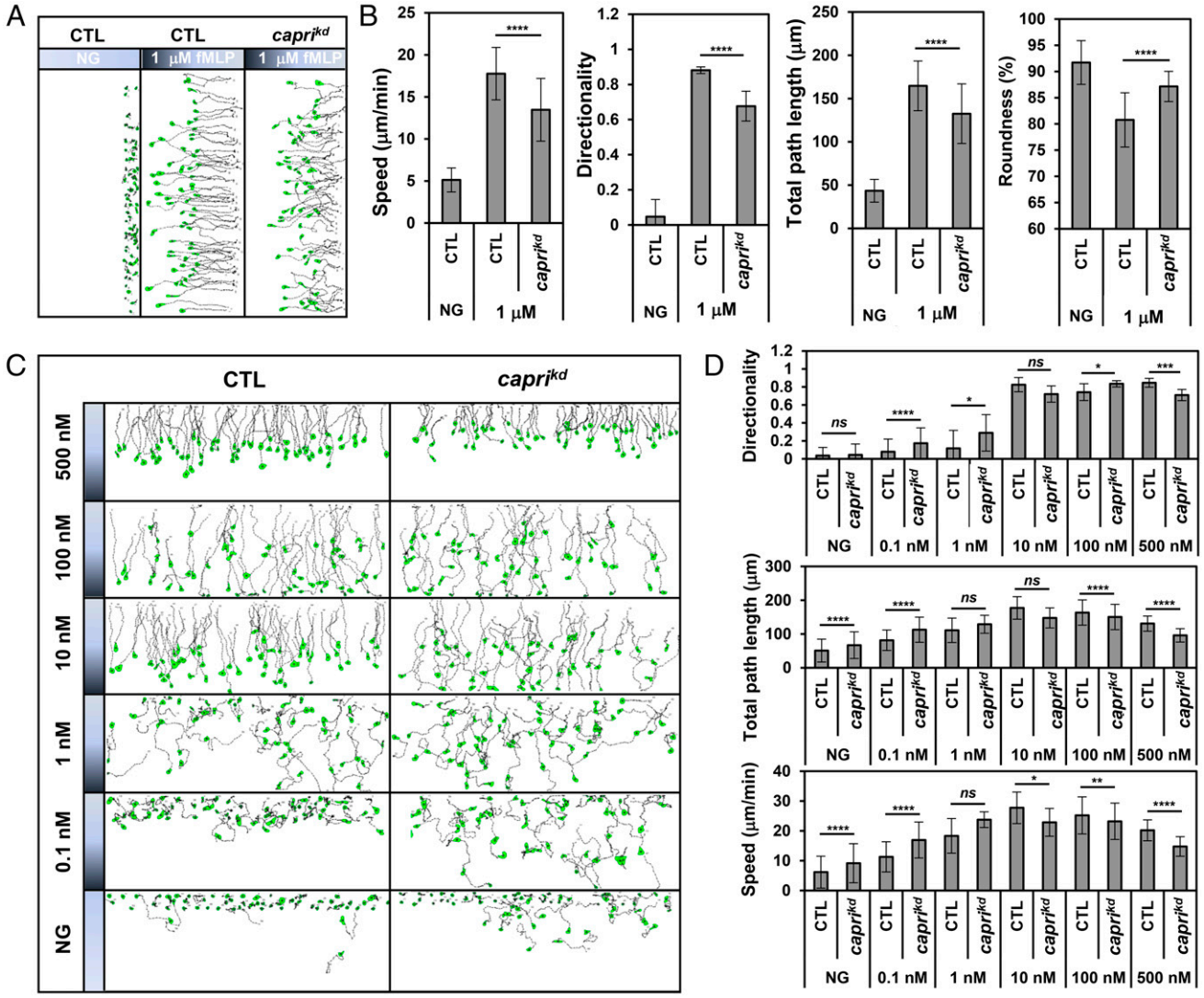

Fig. 6. The concentration range of fMLP gradients in which neutrophils chemotax efficiently is upshifted in *capri*^{kd} cells. (*A*) Montages showing the travel path of chemotaxing CTL or *capri*^{kd} cells in a gradient generated from a 1-μM fMLP source. The plain or shaded panels on top of the images in the montage indicate either no gradient (NG) or 1-μM fMLP gradient. fMLP gradients generated on the terrace are linear gradients. The concentration on the right side of the terrace is 0 and the concentration on the left side of the terrace is 1 μM. Movement of at least 60 cells in each group from multiple independent experiments under the same condition was analyzed by DIAS software and is shown; also refer to Movie S8. The precise chemoattractant concentration (C) of gradient a cell experienced at a given position in *A* and *C* depends on the concentration of the fMLP source (C_{source}) and the ratio between the distance the cell traveled (the traveled length) from 0 concentration to the total distance (the total length) to the fMLP source. That is, $C = C_{source} \times$ ratio of traveled length versus total length. (*B*) Chemotaxis behaviors measured from *A* are described as four parameters: directionality, which is "upward" directionality, in which 0 represents random movement and 1 represents straight movement toward the gradient; speed, defined as the distance that the centroid of the cell moves as a function of time; total path length, the total distance the cell has traveled; and roundness (percent) for polarization, which is calculated as the ratio of the width to the length of the cell. Thus, a circle (no polarization) is 1 and a line (perfect polarization) is 0. A total of 60 cells from each group were measured for 10 and 6.25 min in *B* and *D*, respectively. The mean ± SD was shown. Student's *t* test was used to calculate the *P* values, which are indicated as **** ($P < 0.0001$). (*C*) Montages show the travel path of chemotaxing CTL or *capri*^{kd} cells in response to a wide range of fMLP gradients. The plain or shaded panels on the left side of the images in the montage indicate either NG or fMLP gradient sourced from the indicated concentrations. The concentration on the top side of the terrace is 0, and the concentration at the bottom side of the terrace is as indicated on the left side of the terrace. The movement of at least 60 cells in each group from multiple independent experiments under the same conditions was analyzed by DIAS software and is shown; also refer to Movie S9. (*D*) Chemotaxis behaviors measured from *C* are described by three parameters: directionality, speed, and total path length, as described in *B*. Student's *t* test was used to calculate the *P* values, which are indicated as *ns* (not significant $P > 0.1$), * ($P < 0.1$), ** ($P < 0.01$), *** ($P < 0.001$), or **** ($P < 0.0001$).

continuous translocation of F-tractin–GFP to the protrusion sites (Fig. 8*A*, *Top* and Movie S10, *Left*). In contrast, more than 80% of the *capri*^{kd} cells showed the clear membrane translocation of F-tractin upon 0.1-nM fMLP stimulation (Movie S10, *Right* and Fig. 8*B*), indicating a higher sensitivity of *capri*^{kd} cells. Not surprisingly, 10 nM fMLP induced the robust membrane translocation of F-tractin in both CTL and *capri*^{kd} cells with different dynamics: CTL cells showed a clear, transient translocation of F-tractin–GFP to PM (~5 to 40 s), followed by a withdrawal of most F-tractin from the PM (~50 to 60 s) and then a second translocation to the protrusion sites (>60 s) (Movie S11, *Left*), while *capri*^{kd} cells showed a stronger and longer membrane translocation of F-tractin–GFP to PM (~5 to 90 s) followed by a gradual withdrawal (~90 to 130 s) (Movie S11, *Right*), indicating a stronger response and a longer period of time required to adapt the stimulation. Consistent with the results above, a prolonged,

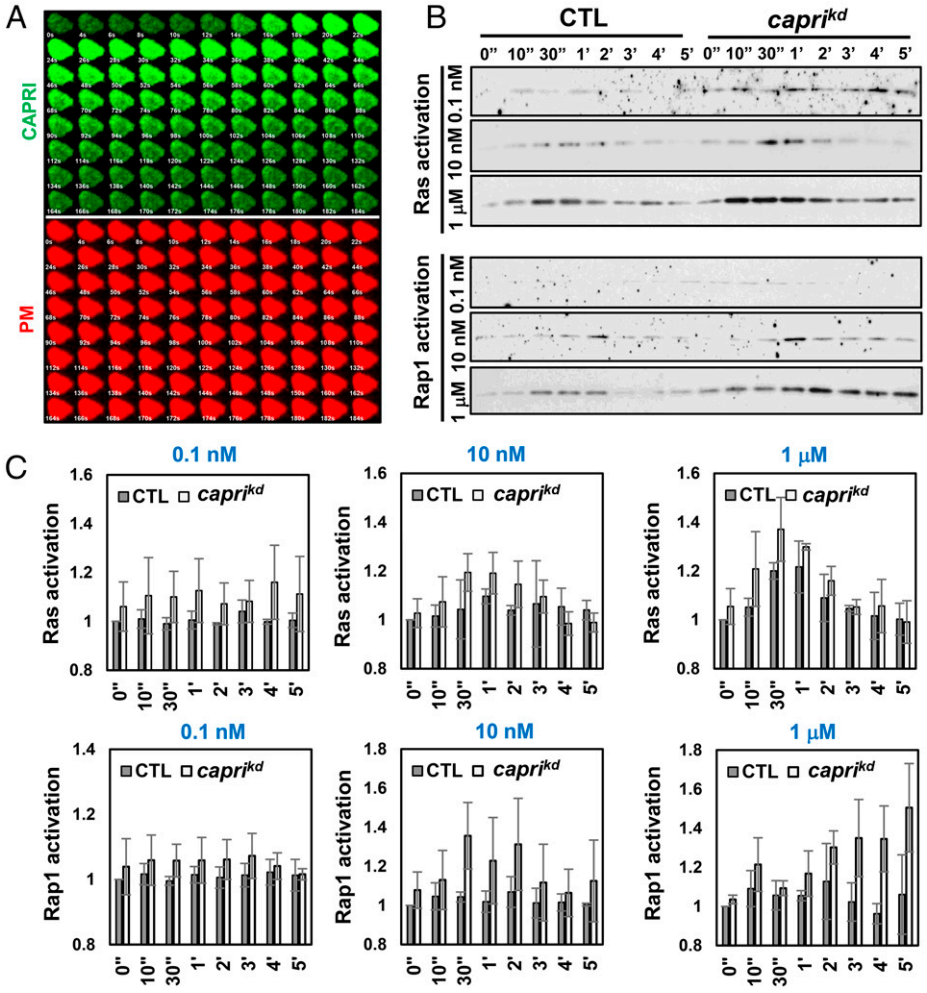

Fig. 7. Activity of Ras and Rap1 is increased in *capri*^{kd} cells. (*A*) CAPRI localizes at the PM before and after fMLP stimulation. (*B*) Ras and Rap1 activation in CTL and *capri*^{kd} cells in response to 0.1-nM, 10-nM, or 1-μM fMLP stimulation determined by a pull-down assay. (*C*) Normalized quantitative densitometry of the active Ras and Rap1 from three independent experiments, including the result presented in *B* and two sets of independent measurements shown in *SI Appendix*, Fig. S17. The intensity ratio of active Ras and Rap1 in WT at time 0 s was normalized to 1. Mean ± SD from the three independent experiments is shown.

nonadaptive actin polymerization was observed in *capri*^{kd} cells in response to stimuli at higher concentrations (Figs. 5 and 8*C*). These results together demonstrate that *capri*^{kd} cells lacking a Ras inhibitor are sensitive to subsensitive-concentration chemoattractant stimuli for CTL cells, while they fail to chemotax through a high-concentration gradient, as CTL cells do.

Discussion

We have previously shown that C2GAP1, a locally recruited Ras inhibitor, mediates Ras adaptation and long-range chemotaxis in *D. discoideum* (16). Here, we show that CAPRI locally controls both Ras adaptation and basal activity and enables human neutrophils to chemotax through a higher-concentration range of chemoattractant gradients.

The Chemoattractant-Induced Deactivation of Ras/Rap1 Is Regulated through Local Membrane Recruitment of CAPRI. CAPRI was first characterized by its calcium dependency on the membrane translocation of CAPRI and the deactivation of Ras (33). Consistent with the above report, we found that CAPRI-ΔC2 did not translocate in response to chemoattractant stimulation (Fig. 2*E*). Like CAPRI, C2GAP1 without the C2 domain also does not translocate in response to cAMP (cyclic AMP, or 3',5'-cyclic adenosine monophosphate) stimulation (16), indicating an essential role of calcium signaling in the membrane targeting of Ras inhibitors in both *Dictyostelium* and human neutrophils. In addition, we found that the ΔPH mutant showed significantly decreased membrane translocation in response to chemoattractant stimulation (Fig. 2 *D* and *E*). This result is consistent with the previous reports that the PH domain of the GAP1 family is responsible for, or plays an important role, in their membrane translocation (34, 39, 57, 58). We also found that the deactivation of GAP activity of the GAP domain (R472A mutant) had no effect on CAPRI's membrane targeting (Fig. 2*D*), although it might affect its interaction with Ras (Fig. 2*E*), consistent with the notion that the arginine residue of the GAP domain not only is responsible for its GAP activity but also stabilizes its interaction with Ras (41). We also found that *capri*$^{kd/OE}$ cells, which displayed little or no Ras activation, still exhibited a strong CAPRI membrane translocation, indicating that the active status of Ras is not required for CAPRI membrane translocation. Unlike CAPRI (33), C2GAP1 without a GAP domain does not translocate upon cAMP stimulation. Nor does C2GAP1 translocate in the cells without interacting with Ras proteins (16). It would be critical to investigate the role of the physical interaction between the GAP domain and Ras in the membrane targeting of C2GAP1 in *Dictyostelium* in the future.

Inhibitor for the GPCR-Mediated Adaptation Regulates the Sensitivity of a Eukaryotic Cell. Motile *Escherichia coli* provides the simplest and the best understood model of the chemosensing system that is also mediated by chemoreceptors (59, 60). The modification of the chemoreceptors and interactions among the chemoreceptors have been proposed for a robust response, a precise adaptation, and a high sensitivity of chemoreceptors in bacteria (61–63). However, the molecular mechanism by which to control the GPCR-mediated adaption and the sensitivity of a

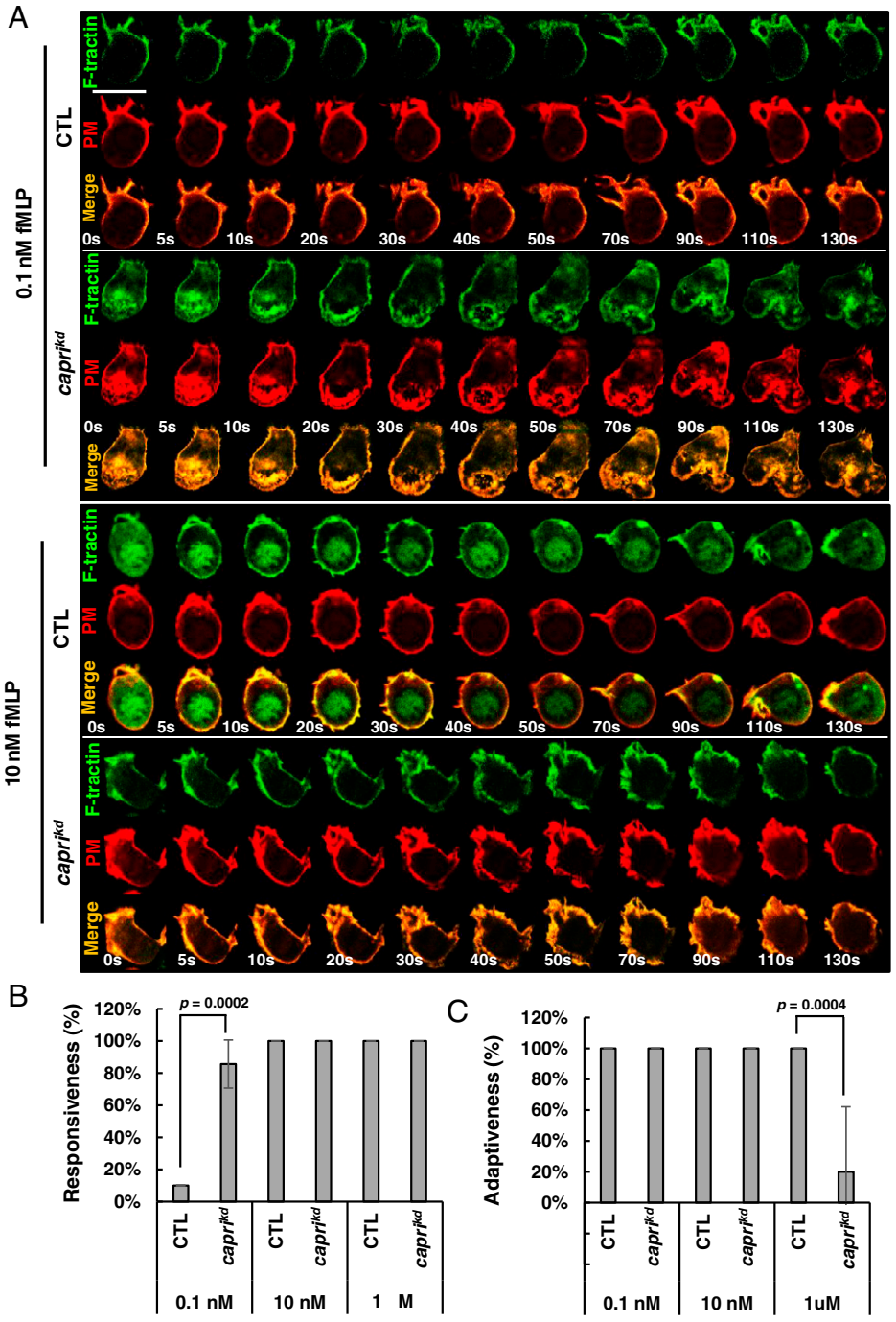

Fig. 8. *capri*^{kd} cells are more sensitive to the stimuli at low concentration and fail to adapt to the stimuli at high concentrations. (*A*) Montage shows cell response as actin polymerization monitored through the membrane translocation of F-actin probe, F-tractin–GFP, in both CTL or *capri*^{kd} HL60 cells using fluorescent microscopy. Cells expressing GFP–F-tractin (green) and PM marker (red) were stimulated with either 0.1- or 10-nM fMLP stimulation. (Scale bar, 10 μm.) Movie S10 is CTL (*Left*) and *capri*^{kd} (*Right*) cells in response to homogeneously applied 0.1-nM fMLP stimulation. Movie S11 is CTL (*Left*) and *capri*^{kd} (*Right*) cells stimulated with homogeneously applied 10 nM fMLP. (*B*) The percentage of cells that respond to the indicated concentration of fMLP stimuli in CTL and *capri*^{kd} cells is shown. (*C*) Percentage of cells with adaptation in response to fMLP stimulation. *B* and *C* were measured with the same sets of data. The numbers of independent experiments for CTL and *capri*^{kd} cells for 0.1-nM, 10-nM, and 1-μM fMLP stimuli are 11 and 7, 8 and 10, and 5 and 9, respectively. Student's *t* test was used to calculate the *P* value.

eukaryotic cell in chemotaxis are not fully understood. A local excitation and global inhibition model explained how a eukaryotic cell responds to chemoattractant stimuli with a wide concentration range, achieves adaptation, and establishes the intracellular polarization (10, 64). Different from *E. coli*, chemoattractant stimulation induces a persistent activation of heterotrimeric G protein in *Dictyostelium* (6, 11, 26), indicating that adaptation occurs downstream of GPCR/G protein in the eukaryotic cell. Recently, the regulators of heterotrimeric G proteins, such as RIC8 (a nonreceptor GEF protein for the Gα subunit) and Gip1 in *Dictyostelium*, and their functions in cAMP gradient sensing and chemotaxis have been revealed (65, 66). We constructed a detailed model to explain the adaptation and chemosensing of *Dictyostelium* cells (15, 67), which led us to uncover the essential role of RasGAPs, the Ras inhibitors, in the GPCR-mediated adaptation (11, 16). Interestingly, cells lacking Ras GAPs, both *capri*^{kd} and *c2gapA*$^{-}$, show higher, basal Ras activity and reach maximum response upon weaker stimuli (Figs. 7 and 8) (16), while cells without essential components for proper G protein activation, such as *ric8*$^{-}$ or *gip1*$^{-}$, require stronger stimuli to reach maximum response (65, 66). Recently, it has been shown that reducing the $PI(3,4)P_2$ level on the PM increases Ras activity and enhances the excitability in *D. discoideum* (18, 19) and that active Ras plays a role in basal locomotion and in chemotaxing through very shallow gradients (24). These reports inspired us to test the chemotaxis capability of both CTL and *capri*^{kd} cells using wide concentration range gradients of various chemoattractants (Fig. 6 and *SI*

Appendix, Fig. S16). In response to fMLP gradients, CTL cells chemotaxed better than *capri*^{kd} cells did in gradients at high concentrations (>100 nM), while they displayed similar chemotaxis capability to *capri*^{kd} cells in mild gradients (10 nM fMLP). In weak gradients (<1 nM), *capri*^{kd} cells chemotaxed better than CTL cells did. Similar chemotaxis behavior was also observed when CTL and *capri*^{kd} cells were exposing to gradients of IL-8. Interestingly, *capri*^{kd} cells sensed and responded to weak gradients of fMLP and IL-8 at the concentration that are subsensitive to CTL cells because of a higher sensitivity of *capri*^{kd} cells (Figs. 7 and 8). Thus, our study provides evidence that human neutrophils locally recruit Ras inhibitor, CAPRI, to regulate Ras adaptation and their sensitivity. CAPRI enables human neutrophils to chemotax through a higher-concentration range of chemoattractant gradients by lowering its sensitivity and by mediating the GPCR-mediated adaptation.

Multiple RasGAP Proteins Might Be Involved in Ras Deactivation in the Chemoattractant-Induced Adaptation of Neutrophils. In the present study, we have shown that CAPRI mediates the chemoattractant-induced Ras adaptation and sensitivity of neutrophils. Similar to *Dictyostelium* cells lacking C2GAP1 (*c2gapA*$^{-}$), human neutrophils without CAPRI fail in chemoattractant-induced, adaptive Ras activation; have significantly increased phosphorylation of downstream effectors, such as AKT, and excessive actin polymerization; and exhibit an impaired chemotaxis in response to high concentrations of chemoattractants. However, in response to a low-concentration (either 0.1 nM or 10 nM fMLP) stimulation, *capri*^{kd} cells displayed transient Ras/Rap1 activation and actin polymerization, although they displayed prolonged, nonadaptive responses upon stimulation with higher concentrations (Figs. 1, 7, and 8). HL60 cells also expressed RASAL1 and RASAL2 (*SI Appendix*, Fig. S2) (37), which also deactivate Ras (34, 39). In mouse and human neutrophils, there are other RasGAP proteins expressed in addition to CAPRI (*SI Appendix*, Fig. S2). p120 GAP is present in both human and mouse neutrophils but absent in HL60 cells (68), and its role has been implicated in cell migration (69, 70). While we revealed a major role of CAPRI in mediating the GPCR-mediated Ras adaptation in HL60 cells, it is also crucial to determine the potential roles of other RasGAP proteins in Ras adaptation and chemotaxis in primary mammalian neutrophils.

Materials and Methods

Cells, Cell Lines, Cell Culture, and Differentiation. Cells were maintained in RPMI 1640 culture medium (RPMI medium 1640 with 10% [volume/volume], fetal bovine serum [FBS], and 25 mM Hepes [Quality Biological, Inc.]) (36). HL60 cells were differentiated in RPMI 1640 culture medium containing 1.3% DMSO for 5 d before the experiments. The cells were incubated at 37 °C in a humidified 5% CO_2 atmosphere.

Plasmids and Transfection of Cells. The plasmids encoding complementary DNA of tGFP-tagged human WT and mutant R472A, ΔC2, and ΔPH of CAPRI, and control tGFP alone were from OriGene. The plasmids of active Ras sensor Raf-binding domain tagged with mRFP (RBD-RFP), GFP-PH-AKT, and PM markers of mem-cerulean, CAAX-mCherry, and C1AC1A-EYFP were from Addgene. F-actin sensor tractin-GFP was obtained from John Hammer, The National Heart, Lung, and Blood Institute (NHLBI), Bethesda, MD (55). The transfection procedure was as previously described (27).

Imaging and Data Processing. Cells were plated and allowed to adhere to the cover glass of a 4-well or a 1-well chamber (Nalge Nunc International) precoated with fibronectin (Sigma-Aldrich) for 10 min and then covered with RPMI medium 1640 with 10% FBS and 25 mM Hepes. For confocal microscopy, cells were imaged using a Carl Zeiss Laser Scanning Microscope Zen 780 (Carl Zeiss) with a Plan-Apochromat 60×/1.4 Oil DIC M27 objective. For the uniform stimulation experiment of membrane translocation assays, the stimuli were directly delivered to the cells, as previously described (27). The micropipette chemotaxis assay was as previously reported (71). To establish a gradient, a Femtotip micropipette is filled with 30 μL of solution containing chemoattractant and a desirable fluorescence dye (either Alexa 488 or Alexa 633) and then attached to the FemtoJet microinjector and micromanipulator. The output pressure of the FemtoJet is set at Pc = 70 hPa to release a constant and tiny volume of the mixture into a 1-well chamber that is filled with 6 mL buffer and cells. Under these conditions, a gradient can be established within 100 μm from the tip of the micropipette and is usually stable for more than 1 h. Images were processed and analyzed with Zen Black software. Images were further processed in Adobe Photoshop (Adobe Systems). The membrane translocation of the indicated protein was measured by the depletion of the interested protein in the cytoplasm. The data obtained were further analyzed with Microsoft Office Excel. For a quantitative analysis of membrane translocation dynamics of the indicated molecules, the cytosolic depletion of the indicated molecule was measured. Regions of interest (ROIs) in the cytoplasm (avoiding the nucleus area as much as possible) were within the cells throughout the time period of the measurements. The periphery of the cell was marked by the membrane markers. For data analysis, to normalize the effect of photobleaching during data acquisition, the intensity of ROIs in the cytoplasm was first divided by the intensity of whole cells at each given time point. To normalize the effect of morphological change during the time period, the above resulting data were divided by the intensity of ROIs in PM marker channel. Lastly, the resulting data were divided by that at time 0 s; consequently, the relative intensity of any cells at time 0 s became 1. The graph of mean ± SD is shown. TIRF microscopy was done using a Nikon microscope, as previously described, to image GFP- and mCherry-tagged proteins (15). GFP and mCherry were excited by the 488-nm and 561-nm laser lines, respectively. The evanescent field was obtained by an HP Apo TIRF 100× objective lens with a numerical aperture 1.49 (Nikon). Fluorescence emission was collected through band-pass filters: a 525/50-nm emission filter for GFP and a 600/50-nm emission filter for mCherry, respectively, onto an Andor iXon Ultra CCD camera. Imaging data were acquired by software, NIS (Nikon Imaging System), and further analyzed using Image J-Fuji.

TAXIScan Chemotaxis Assay and Data Analysis. The procedure was as previously reported (56). Briefly, differentiated cells were loaded onto one side of fibronectin-coated 4-μm EZ-TAXIScan chambers. The chemoattractants at the indicated concentrations were added to the other side of the well across the terrace to generate a liner gradient in which the cells chemotax through. The traveled distance is the traveled length (micrometers). The length of terrace is the total length of the gradient generated (260 μm). The chemoattractant concentration of gradient (C) cell experienced at the each give position depends on both the concentration of fMLP source (C_{source}) and the distance they traveled (the traveled length) from no gradient to the total distance (the total length) to the fMLP source. That is, $C = C_{source} \times$ ratio of the traveled length versus the total length. The cells migrated for 30 min at 37 °C. Images were taken for 30 min at 15-s intervals. For chemotaxis parameter measurements, 20 cells in each group were analyzed with DIAS software (72). Chemotaxis behaviors measured from Fig. 6*A* are described as four parameters : directionality, which is "upward" directionality, in which 0 represents random movement and 1 represents straight movement toward the gradient; speed, defined as the distance that the centroid of the cell moves as a function of time; total path length, the total distance the cell has traveled; and roundness (percent) for polarization, which is calculated as the ratio of the width to the length of the cell. Thus, a circle (no polarization) is 1 and a line (perfect polarization) is 0. A total of 20 cells from each group were measured and the mean ± SD was shown. Student's *t* test was used to calculate the *P* values. In Fig. 6 *A–D*, cells were traced for 10 and 6.26 min, respectively. The bar graphs of chemotaxis parameters in mean and SD were plotted with Microsoft Office Excel.

Detailed descriptions of the establishment of stable *capri* knockdown cell, the purification of human and mouse neutrophils, reagents and antibodies, plasmids and the transfection of cells, immunoblotting of fMLP-mediated signaling components, Ras and Rap1 activation assay, actin polymerization assay, immunoprecipitation assay, and SiR-actin staining are provided in *SI Appendix*. To access CAPRI-related plasmids and the data in the paper, please address requests to addgene.com and xxu@niaid.nih.gov, respectively.

Data Availability. Some study data are available.

ACKNOWLEDGMENTS. We thank Dr. Arjan Kortholt, Dr. Xinzhuan Su, and Dr. Peter Crompton for critical reading of the article. This work was supported by the NIH Intramural Fund from the National Institute of Allergy and Infectious Diseases, NIH.

1. S. Nourshargh, R. Alon, Leukocyte migration into inflamed tissues. *Immunity* **41**, 694–707 (2014).

2. C. Tecchio, A. Micheletti, M. A. Cassatella, Neutrophil-derived cytokines: Facts beyond expression. *Front. Immunol.* **5**, 508 (2014).

3. A. Mantovani, M. A. Cassatella, C. Costantini, S. Jaillon, Neutrophils in the activation and regulation of innate and adaptive immunity. *Nat. Rev. Immunol.* **11**, 519–531 (2011).
4. E. Kolaczkowska, P. Kubes, Neutrophil recruitment and function in health and inflammation. *Nat. Rev. Immunol.* **13**, 159–175 (2013).
5. O. Hoeller, D. Gong, O. D. Weiner, How to understand and outwit adaptation. *Dev. Cell* **28**, 607–616 (2014).
6. C. Janetopoulos, T. Jin, P. Devreotes, Receptor-mediated activation of heterotrimeric G-proteins in living cells. *Science* **291**, 2408–2411 (2001).
7. P. Devreotes, C. Janetopoulos, Eukaryotic chemotaxis: Distinctions between directional sensing and polarization. *J. Biol. Chem.* **278**, 20445–20448 (2003).
8. A. R. Houk *et al.*, Membrane tension maintains cell polarity by confining signals to the leading edge during neutrophil migration. *Cell* **148**, 175–188 (2012).
9. A. Nakajima, S. Ishihara, D. Imoto, S. Sawai, Rectified directional sensing in long-range cell migration. *Nat. Commun.* **5**, 5367 (2014).
10. C. A. Parent, P. N. Devreotes, A cell's sense of direction. *Science* **284**, 765–770 (1999).
11. X. Xu, M. Meier-Schellersheim, J. Yan, T. Jin, Locally controlled inhibitory mechanisms are involved in eukaryotic GPCR-mediated chemosensing. *J. Cell Biol.* **178**, 141–153 (2007).
12. K. Takeda *et al.*, Incoherent feedforward control governs adaptation of activated Ras in a eukaryotic chemotaxis pathway. *Sci. Signal.* **5**, ra2 (2012).
13. W. Ma, A. Trusina, H. El-Samad, W. A. Lim, C. Tang, Defining network topologies that can achieve biochemical adaptation. *Cell* **138**, 760–773 (2009).
14. P. G. Charest *et al.*, A Ras signaling complex controls the RasC-TORC2 pathway and directed cell migration. *Dev. Cell* **18**, 737–749 (2010).
15. X. Xu *et al.*, Coupling mechanism of a GPCR and a heterotrimeric G protein during chemoattractant gradient sensing in *Dictyostelium*. *Sci. Signal.* **3**, ra71 (2010).
16. X. Xu *et al.*, GPCR-controlled membrane recruitment of negative regulator C2GAP1 locally inhibits Ras signaling for adaptation and long-range chemotaxis. *Proc. Natl. Acad. Sci. U.S.A.* **114**, E10092–E10101 (2017).
17. S. Zhang, P. G. Charest, R. A. Firtel, Spatiotemporal regulation of Ras activity provides directional sensing. *Curr. Biol.* **18**, 1587–1593 (2008).
18. X. Li *et al.*, Mutually inhibitory Ras-PI(3,4)P_2 feedback loops mediate cell migration. *Proc. Natl. Acad. Sci. U.S.A.* **115**, E9125–E9134 (2018). Correction in: *Proc. Natl. Acad. Sci. U.S.A.* **115**, E10286 (2018).
19. Y. Miao *et al.*, Altering the threshold of an excitable signal transduction network changes cell migratory modes. *Nat. Cell Biol.* **19**, 329–340 (2017).
20. A. T. Sasaki, C. Chun, K. Takeda, R. A. Firtel, Localized Ras signaling at the leading edge regulates PI3K, cell polarity, and directional cell movement. *J. Cell Biol.* **167**, 505–518 (2004).
21. S. Suire *et al.*, GPCR activation of Ras and PI3Kc in neutrophils depends on PLCb2/b3 and the RasGEF RasGRP4. *EMBO J.* **31**, 3118–3129 (2012).
22. M.-J. Wang, Y. Artemenko, W.-J. Cai, P. A. Iglesias, P. N. Devreotes, The directional response of chemotactic cells depends on a balance between cytoskeletal architecture and the external gradient. *Cell Rep.* **9**, 1110–1121 (2014).
23. L. Zheng, J. Eckerdal, I. Dimitrijevic, T. Andersson, Chemotactic peptide-induced activation of Ras in human neutrophils is associated with inhibition of p120-GAP activity. *J. Biol. Chem.* **272**, 23448–23454 (1997).
24. P. J. van Haastert, I. Keizer-Gunnink, A. Kortholt, Coupled excitable Ras and F-actin activation mediates spontaneous pseudopod formation and directed cell movement. *Mol. Biol. Cell* **28**, 922–934 (2017).
25. R. H. Insall, J. Borleis, P. N. Devreotes, The aimless RasGEF is required for processing of chemotactic signals through G-protein-coupled receptors in *Dictyostelium*. *Curr. Biol.* **6**, 719–729 (1996).
26. X. Xu, M. Meier-Schellersheim, X. Jiao, L. E. Nelson, T. Jin, Quantitative imaging of single live cells reveals spatiotemporal dynamics of multistep signaling events of chemoattractant gradient sensing in *Dictyostelium*. *Mol. Biol. Cell* **16**, 676–688 (2005).
27. X. Xu *et al.*, Quantitative monitoring spatiotemporal activation of Ras and PKD1 using confocal fluorescent microscopy. *Methods Mol. Biol.* **1407**, 307–323 (2016).
28. H. Kae, C. J. Lim, G. B. Spiegelman, G. Weeks, Chemoattractant-induced Ras activation during *Dictyostelium* aggregation. *EMBO Rep.* **5**, 602–606 (2004).
29. S. Suire *et al.*, Gbetagammas and the Ras binding domain of p110gamma are both important regulators of PI(3)Kgamma signalling in neutrophils. *Nat. Cell Biol.* **8**, 1303–1309 (2006).
30. C. Knall *et al.*, Interleukin-8 regulation of the Ras/Raf/mitogen-activated protein kinase pathway in human neutrophils. *J. Biol. Chem.* **271**, 2832–2838 (1996).
31. S. Yarwood, D. Bouyoucef-Cherchalli, P. J. Cullen, S. Kupzig, The GAP1 family of GTPase-activating proteins: Spatial and temporal regulators of small GTPase signalling. *Biochem. Soc. Trans.* **34**, 846–850 (2006).
32. T. Grewal, M. Koese, F. Tebar, C. Enrich, Differential regulation of RasGAPs in cancer. *Genes Cancer* **2**, 288–297 (2011).
33. P. J. Lockyer, S. Kupzig, P. J. Cullen, CAPRI regulates Ca(2+)-dependent inactivation of the Ras-MAPK pathway. *Curr. Biol.* **11**, 981–986 (2001).
34. P. J. Lockyer *et al.*, Identification of the ras GTPase-activating protein GAP1(m) as a phosphatidylinositol-3,4,5-trisphosphate-binding protein in vivo. *Curr. Biol.* **9**, 265–268 (1999).
35. J. Zhang, J. Guo, I. Dzhagalov, Y.-W. He, An essential function for the calcium-promoted Ras inactivator in Fcgamma receptor-mediated phagocytosis. *Nat. Immunol.* **6**, 911–919 (2005).
36. X. Xu *et al.*, GPCR-mediated PLCβγ/PKCβ/PKD signaling pathway regulates the cofilin phosphatase slingshot 2 in neutrophil chemotaxis. *Mol. Biol. Cell* **26**, 874–886 (2015).
37. E. Rincón, B. L. Rocha-Gregg, S. R. Collins, A map of gene expression in neutrophil-like cell lines. *BMC Genomics* **19**, 573 (2018).
38. M. Upadhyaya *et al.*, Mutational and functional analysis of the neurofibromatosis type 1 (NF1) gene. *Hum. Genet.* **99**, 88–92 (1997).
39. Q. Liu *et al.*, CAPRI and RASAL impose different modes of information processing on Ras due to contrasting temporal filtering of Ca2+. *J. Cell Biol.* **170**, 183–190 (2005).
40. I. R. Vetter, A. Wittinghofer, The guanine nucleotide-binding switch in three dimensions. *Science* **294**, 1299–1304 (2001).
41. K. Scheffzek, A. Lautwein, W. Kabsch, M. R. Ahmadian, A. Wittinghofer, Crystal structure of the GTPase-activating domain of human p120GAP and implications for the interaction with Ras. *Nature* **384**, 591–596 (1996).
42. X. Xu, P. Johnson, S. C. Mueller, Breast cancer cell movement: Imaging invadopodia by TIRF and IRM microscopy. *Methods Mol. Biol.* **571**, 209–225 (2009).
43. Z. Li *et al.*, Roles of PLC-beta2 and -beta3 and PI3Kgamma in chemoattractant-mediated signal transduction. *Science* **287**, 1046–1049 (2000).
44. G. Servant *et al.*, Polarization of chemoattractant receptor signaling during neutrophil chemotaxis. *Science* **287**, 1037–1040 (2000).
45. W. Tang *et al.*, A PLCβ/PI3Kγ-GSK3 signaling pathway regulates cofilin phosphatase slingshot2 and neutrophil polarization and chemotaxis. *Dev. Cell* **21**, 1038–1050 (2011).
46. H. Cai *et al.*, Ras-mediated activation of the TORC2-PKB pathway is critical for chemotaxis. *J. Cell Biol.* **190**, 233–245 (2010).
47. D. D. Sarbassov, D. A. Guertin, S. M. Ali, D. M. Sabatini, Phosphorylation and regulation of Akt/PKB by the rictor-mTOR complex. *Science* **307**, 1098–1101 (2005).
48. D. R. Alessi *et al.*, Mechanism of activation of protein kinase B by insulin and IGF-1. *EMBO J.* **15**, 6541–6551 (1996).
49. K. Mizuno, Signaling mechanisms and functional roles of cofilin phosphorylation and dephosphorylation. *Cell. Signal.* **25**, 457–469 (2013).
50. H. Kitayama, Y. Sugimoto, T. Matsuzaki, Y. Ikawa, M. Noda, A ras-related gene with transformation suppressor activity. *Cell* **56**, 77–84 (1989).
51. J. L. Bos, All in the family? New insights and questions regarding interconnectivity of Ras, Rap1 and Ral. *EMBO J.* **17**, 6776–6782 (1998).
52. T. G. Bivona *et al.*, Rap1 up-regulation and activation on plasma membrane regulates T cell adhesion. *J. Cell Biol.* **164**, 461–470 (2004).
53. T. J. Jeon, D.-J. Lee, S. Merlot, G. Weeks, R. A. Firtel, Rap1 controls cell adhesion and cell motility through the regulation of myosin II. *J. Cell Biol.* **176**, 1021–1033 (2007).
54. Y. Dai *et al.*, Ca^{2+}-dependent monomer and dimer formation switches CAPRI Protein between Ras GTPase-activating protein (GAP) and RapGAP activities. *J. Biol. Chem.* **286**, 19905–19916 (2011).
55. J. Yi, X. S. Wu, T. Crites, J. A. Hammer III, Actin retrograde flow and actomyosin II arc contraction drive receptor cluster dynamics at the immunological synapse in Jurkat T cells. *Mol. Biol. Cell* **23**, 834–852 (2012).
56. X. Wen, T. Jin, X. Xu, Imaging G protein-coupled receptor-mediated chemotaxis and its signaling events in neutrophil-like HL60 cells. *J. Vis. Exp.* **115**, 54511 (2016).
57. P. J. Lockyer *et al.*, Distinct subcellular localisations of the putative inositol 1,3,4,5-tetrakisphosphate receptors GAP1IP4BP and GAP1m result from the GAP1IP4BP PH domain directing plasma membrane targeting. *Curr. Biol.* **7**, 1007–1010 (1997).
58. G. E. Cozier *et al.*, GAP1IP4BP contains a novel group I pleckstrin homology domain that directs constitutive plasma membrane association. *J. Biol. Chem.* **275**, 28261–28268 (2000).
59. J. S. Parkinson, G. L. Hazelbauer, J. J. Falke, Signaling and sensory adaptation in *Escherichia coli* chemoreceptors: 2015 update. *Trends Microbiol.* **23**, 257–266 (2015).
60. S. L. Porter, G. H. Wadhams, J. P. Armitage, Signal processing in complex chemotaxis pathways. *Nat. Rev. Microbiol.* **9**, 153–165 (2011).
61. C. H. Hansen, R. G. Endres, N. S. Wingreen, Chemotaxis in *Escherichia coli*: A molecular model for robust precise adaptation. *PLOS Comput. Biol.* **4**, e1 (2008).
62. B. A. Mello, Y. Tu, Effects of adaptation in maintaining high sensitivity over a wide range of backgrounds for *Escherichia coli* chemotaxis. *Biophys. J.* **92**, 2329–2337 (2007).
63. D. Clausznitzer, O. Oleksiuk, L. Løvdok, V. Sourjik, R. G. Endres, Chemotactic response and adaptation dynamics in *Escherichia coli*. *PLOS Comput. Biol.* **6**, e1000784 (2010).
64. Y. Xiong, C.-H. Huang, P. A. Iglesias, P. N. Devreotes, Cells navigate with a local-excitation, global-inhibition-biased excitable network. *Proc. Natl. Acad. Sci. U.S.A.* **107**, 17079–17086 (2010).
65. Y. Kamimura, Y. Miyanaga, M. Ueda, Heterotrimeric G-protein shuttling via Gip1 extends the dynamic range of eukaryotic chemotaxis. *Proc. Natl. Acad. Sci. U.S.A.* **113**, 4356–4361 (2016).
66. R. Kataria *et al.*, *Dictyostelium* Ric8 is a nonreceptor guanine exchange factor for heterotrimeric G proteins and is important for development and chemotaxis. *Proc. Natl. Acad. Sci. U.S.A.* **110**, 6424–6429 (2013).
67. M. Meier-Schellersheim *et al.*, Key role of local regulation in chemosensing revealed by a new molecular interaction-based modeling method. *PLOS Comput. Biol.* **2**, e82 (2006).
68. T. Skorski *et al.*, p120 GAP requirement in normal and malignant human hematopoiesis. *J. Exp. Med.* **178**, 1923–1933 (1993).
69. T. Grewal, C. Enrich, Molecular mechanisms involved in Ras inactivation: The annexin A6-p120GAP complex. *BioEssays* **28**, 1211–1220 (2006).
70. T. Grewal *et al.*, Annexin A6-A multifunctional scaffold in cell motility. *Cell Adhes. Migr.* **11**, 288–304 (2017).
71. X. Xu, J. A. Brzostowski, T. Jin, Monitoring dynamic GPCR signaling events using fluorescence microscopy, FRET imaging, and single-molecule imaging. *Methods Mol. Biol.* **571**, 371–383 (2009).
72. D. Wessels *et al.*, A computer-assisted system for reconstructing and interpreting the dynamic three-dimensional relationships of the outer surface, nucleus and pseudopods of crawling cells. *Cell Motil. Cytoskeleton* **41**, 225–246 (1998).